Planetary and Space Science 194 (2020) 105104

Contents lists available at ScienceDirect

Planetary and Space Science

journal homepage: www.elsevier.com/locate/pss

Concerning the interaction of a transmitted interplanetary impulse with a plasmaspheric drainage plume: First results from 3-D hybrid kinetic modeling

A.S. Lipatov [a,b,*,1], D.G. Sibeck [c,1]

[a] GPHI UMBC/NASA GSFC, Code 673, Greenbelt, MD, 20771, USA
[b] Faculty of Problems of Physics and Power Engineering, Moscow Institute of Physics and Technology, Russia
[c] NASA Goddard Space Flight Center, Code 674, Greenbelt, MD, 20771, USA

ARTICLE INFO

Keywords:
Solar wind
Magnetosphere
Plasmasphere
Radiation belts
Ring current
Interplanetary shocks and transmitted impulses

ABSTRACT

We present a new hybrid kinetic model to simulate the response of plasmaspheric drainage plumes to impulsive interplanetary pressure pulses. Since particle distributions attending the interplanetary pulses and in the drainage plume are non-Maxwellian, wave-particle interactions play a crucial role in energy transport within and outside the plumes. Finite gyroradius effects become important in mass loading of the transmitted impulse with the drainage plume ions. A forward-reverse shock structure develops from the initial step-like transmitted shock. First results show that the impulse causes strong deformations in the global structure of the plume. The anisotropic ion velocity distribution functions at the impulse front and inside the plume help us determine energy transport via wave-particle interactions throughout the Earth's inner magnetosphere.

1. Introduction

Solar wind shocks striking the magnetosphere provide an excellent example of one fundamental mode of interaction between the solar wind and magnetosphere, just as interesting and important as magnetic field reconnection (Cattell et al., 2017; Zhang et al., 2012).

The interaction of interplanetary (IP) shocks (usually fast forward shocks) with the magnetosphere includes several phases, including interaction with the bow shock, transmission through the magnetosheath, interaction with the magnetopause, transmission into the magnetosphere as fast and intermediate mode waves, modifications of the field-aligned and ionospheric current systems, and perturbations in ground magnetograms (Samsonov et al., 2007).

The Earth's inner magnetosphere presents a complex plasma system which includes several plasma structures - the ring current, outer radiation belt, plasmasphere, and inner radiation belt, as shown in Fig. 5 of Mauk et al. (2013). Plasmaspheric plumes are large-scale density structures that are usually connected to the main body of the plasmasphere, and extend outward (e.g., Elphic et al. (1996), Ober et al. (1997), Sandel et al. (2001)). Plasmaspheric plumes have been detected by in-situ and ground-based instruments (e.g., [Chappell et al. (1970), Foster et al. (2002), Moldwin et al. (2004), Goldstein et al. (2004), Darrouzet et al., 2006, 2009). Spacecraft in geosynchronous orbit identify the plumes as regions of dense plasmaspheric plasma advecting sunward toward the dayside magnetopause.

Long-lived plasmaspheric drainage plumes occur during high-speed-stream-driven storms (Borovsky and Denton, 2006; Borovsky et al., 2014). Dense (> 10 cm^{-3}) plasmaspheric plumes and/or cold ions at the magnetopause have been reported in [Chappell (1974), Gosling et al. (1991), McFadden et al. (2008), Zhang et al. 58]. Zhang et al. (2012) suggested the topology of one plasmaspheric plume (see Fig. 5 of Zhang et al. (2012)). The plume density falls with distance from the plasmapause (Zhang et al., 2012).

Darrouzet et al. (2008) presented a statistical analysis of the plasmaspheric plumes observed by the Cluster spacecraft. They found that most plasmaspheric plumes occur for moderate Kp and not for small Dst. They also showed that plumes are mainly located in the afternoon and pre-midnight MLT sectors.

The plasmaspheric plume-transmitted impulse interaction may result in non-Maxwellian ion VDF's that can trigger electromagnetic ion cyclotron (EMIC) waves, toroidal, and poloidal pulsations within magnetosphere (Usanova et al., 2008; Claudepierre et al., 2013; Tsuji

* Corresponding author. GPHI UMBC/NASA GSFC, Code 673, Greenbelt, MD, 20771, USA.
E-mail addresses: Alexander.Lipatov-1@nasa.gov (A.S. Lipatov), David.G.Sibeck@nasa.gov (D.G. Sibeck).
[1] Additional information about the second and third authors.

https://doi.org/10.1016/j.pss.2020.105104
Received 31 March 2019; Received in revised form 12 September 2020; Accepted 20 September 2020
Available online 25 September 2020

et al., 2017). The transmitted shock waves may possibly also heat and accelerate particles in the plasmaspheric plume, ring current and radiation belt.

MHD simulations of interplanetary shock propagation through the inner magnetosphere (Samsonov et al., 2007, 2011, 2014; Kress et al., 2008; Halford et al., 2015) show that the transmitted shock wave front has a step-like form. The thickness of the front is controlled by numerical diffusion. MHD simulations predict the shock propagation speed and its interaction with the plasmapause. However, the dynamics of the shock wave transition are essential to understand the wave-particle interaction between the transmitted shock (impulse) and plasma structures inside the inner magnetosphere.

Since the particle distributions inside the transmitted interplanetary shock waves (impulses), ring current and radiation belts are essentially non-Maxwellian, wave-particle interactions play a very important role in the energy transport that occurs inside the inner magnetosphere. Finite ion gyroradius effects may be important in mass loading the transmitted impulse with the background plasma in the presence of higher energy ions and electrons from the ring current and radiation belts. To study these phenomena, we need a global hybrid code model. We use this model to study a shock front striking the magnetosphere.

Electromagnetic ion cyclotron (EMIC) waves are generated by ion temperature anisotropies ($T_\perp > T_\parallel$) (e.g. Cornwall (1965)). The frequency of EMIC waves is below the local proton gyrofrequency. In the magnetosphere, it ranges from 0.1 to 5 Hz. EMIC waves in the hydrogen band (with frequencies between the helium and hydrogen gyrofrequencies) and helium band (with frequencies between the oxygen and helium gyrofrequencies) are often observed in the magnetosphere (Young et al., 1981; Roux et al., 1982; Anderson et al., 1992). Their highest occurrence is in the dayside magnetosphere beyond L = 7 (Anderson et al., 1992). EMIC waves are often associated with magnetospheric compressions (Anderson and Hamilton, 1993; Engebretson et al., 2002; Usanova et al., 2008).

Zhang et al. (2012) report a case study of the global response of the geospace plasma environment to an interplanetary (IP) shock that was observed at 02:24 UT on May 28, 2008 by the multiple THEMIS spacecraft in the magnetosheath (THEMIS B and C), the mid-afternoon magnetosphere (THEMIS A), and the dusk magnetosphere (THEMIS D and E). They showed that the interaction between the transmitted IP shock and the magnetosphere has global effects. THEMIS A observations indicate that the IP shock changed the properties of a plasmaspheric plume significantly. The plasmaspheric plume density increased rapidly from 10 to 100cm^{-3} in 4 min and the ion velocity distribution changed from an isotropic to a strongly anisotropic distribution. The plasma and magnetic field observations were obtained from the Electrostatic Analyzer (McFadden et al., 2008), and the Fluxgate magnetometer (Auster et al., 2008) on the THEMIS spacecraft (Angelopoulos, 2008).

In this paper, we use 3-D hybrid-kinetic modeling to investigate the local response of the plasmaspheric plume to an IP shock. Our investigation is directly motivated by the THEMIS spacecraft observations. We compare our predictions with THEMIS-A, D and E spacecraft observations in the mid-afternoon magnetosphere, and observations in the dusk magnetosphere (THEMIS D and E) on May 28, 2008/02:00–03:00 in the mid-afternoon magnetosphere (Fig. 4 of Zhang et al. (2012)). We consider several scenarios with various transmitted impulses to see how the shock speed may affect the interaction between the transmitted impulse and the plume. The outline of this paper is as follows. Section 2 presents the simulation model. Section 3 describes results from the model. The last section provides the conclusions of our research.

2. Computational model

We use a quasi-neutral implicit hybrid model (Sect. 2.2.3.1 from Lipatov (2002)), namely, a kinetic description for the ions in the background plasma and plasmaspheric plume, and a fluid approximation for electrons to study the interaction between the transmitted impulse and the inner magnetosphere. This model describes the wave-particle interactions on ion spatial and time scales ($\rho_{ci} = U_0/\Omega_i$ and $\omega \le \Omega_i$) very well, where ρ_{ci} is the gyroradius for ions. U_0 and Ω_i denote the velocity of the shock front and the ion gyrofrequency.

Fig. 1 illustrates of the computational domain, the initial position of the transmitted impulse and the plasmaspheric plume.

We assume that the mass of the background and plume ion populations under consideration are $M_1 = M_p$ and $M_2 = 2M_p$ where M_p is the mass of a proton and the charge states are $Z_1 = 1$ and $Z_2 = 1$. The value of the plume ion mass was chosen as an average mass for a plume with the following composition: 85% (H^+); 10% (He^+); 5% (O^+). In this paper we use a particle-mesh model for ion dynamics instead of the Vlasov/Boltzmann equation.

Single ion particle motion is described by the equations:

$$\frac{d\mathbf{r}_{s,l}}{dt} = \mathbf{v}_{s,l} \tag{1}$$

and

$$\frac{d\mathbf{v}_{s,l}}{dt} = \frac{e}{M_s}\left(\mathbf{E} + \frac{\mathbf{v}_{s,l} \times \mathbf{B}}{c}\right). \tag{2}$$

The subscript s denotes the ion population ($s = 1, 2$ for background and plasmaspheric plume ions). The index l is the individual particle index in the frame of the particle-in-cell method.

In the nonradiative limit, Ampère's law is given by

$$\frac{4\pi}{c}\mathbf{J} = \nabla \times \mathbf{B}; \tag{3}$$

and the induction equation (Faraday's law) by

$$\frac{1}{c}\frac{\partial \mathbf{B}}{\partial t} + \nabla \times \mathbf{E} = 0. \tag{4}$$

The total current is given by

$$\mathbf{J} = \mathbf{J}_e + \mathbf{J}_i; \quad \mathbf{J}_i = \sum_{s=1}^{N_{species}} Z_s e n_s \langle \mathbf{v}_s \rangle = \sum_{s=1}^{N_{species}} e n_s \mathbf{U}_s = e n_i \mathbf{U}_i, \tag{5}$$

where $\mathbf{U}_s$ is the bulk velocity and n_s is the density of ions of type s; $\langle\rangle$ denotes the average value of the ion macro-particle velocities over the cell, n_i is the total ion density, and U_i is the average ion bulk velocity.

The electron density is computed from the quasi-neutrality condition

$$n_e = n_{BG} + n_{plume} \tag{6}$$

Here, n_{BG} and n_{plume} denote the ion densities in the background plasma and plasmaspheric plume.

For massless electrons the equation of motion of the electron fluid takes the form of the standard generalized Ohm's law (e.g. (Braginskii and Leontovich, 1965)):

$$\mathbf{E} = \frac{\mathbf{J}_e \times \mathbf{B}}{e n_e c} - \frac{\nabla p_e}{e n_e} \tag{7}$$

where $p_e = n m_e \langle v_e' 2\rangle/3 = n_e T_e$ is the scalar electron pressure, and v_e' is the thermal velocity of electrons; the electron current J_e is estimated from Eq. (6).

For simplicity we assume that the total electron pressure can be represented as the sum of the partial pressures of all the electron populations:

$$p_e = p_{e0}\frac{\left(\beta_e n_{BG}^{5/3} + \beta_{e,plume} n_{plume}^{5/3}\right)}{\beta_e n_0^{5/3}}, \tag{8}$$

where β_e and $\beta_{e,plume}$ denote the electron background and plasmaspheric plume beta parameters. p_{e0} and n_0 are the background electron pressure

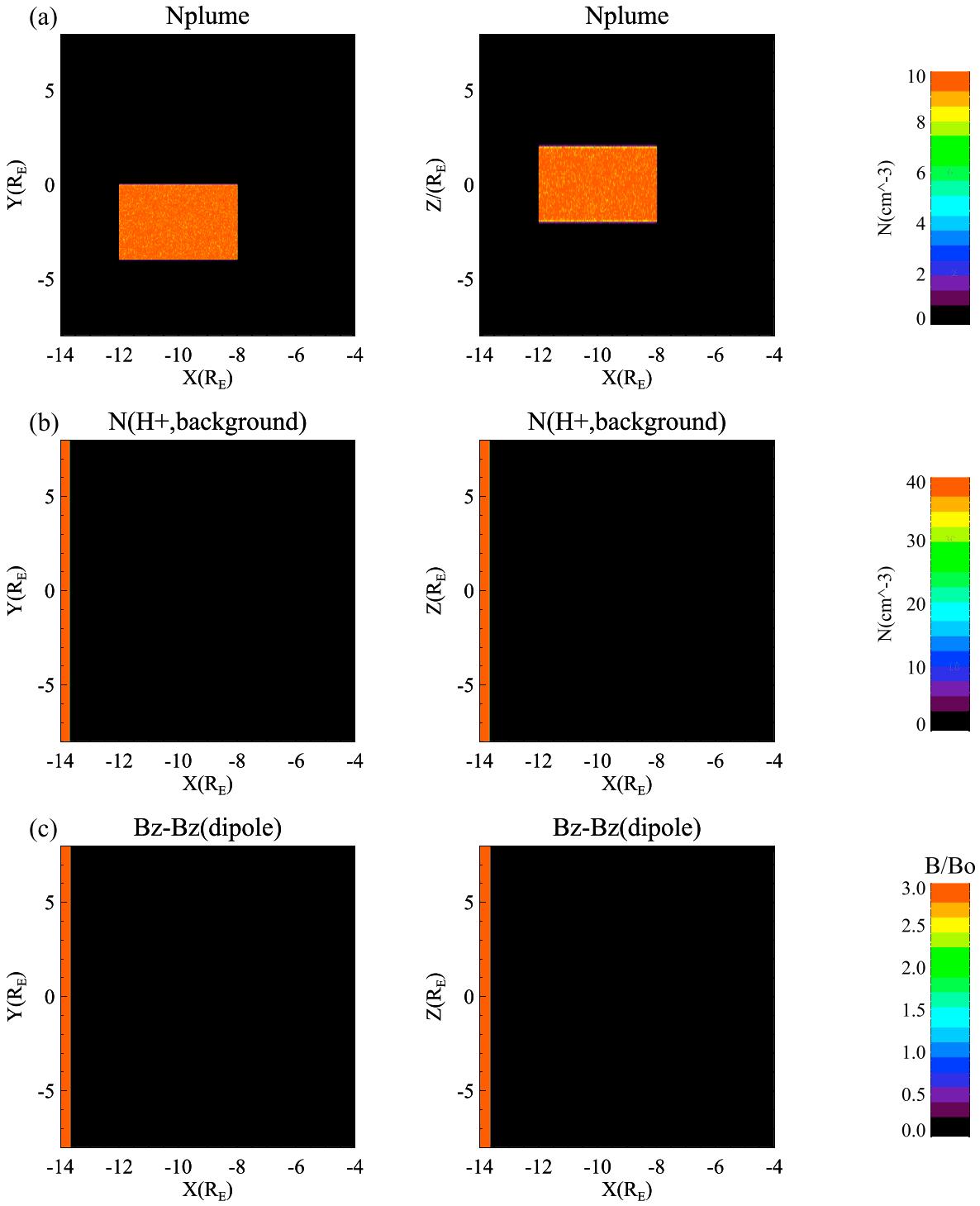

Fig. 1. Initial Conditions. 2-D cuts of plume ($M_i = 2M_p, Z = +1$), impulse ion density and magnetic field ($B_z - B_{z,\mathrm{dipole}}$) profiles in x-y and y-z and x-z planes. The transmitted shock has a step-function profile and it was setup at the left boundary (red-density, green-magnetic field). $U_{\mathrm{downstream}} = 2000$ km/s, $N_2/N_1 = 4$, $B_{z2}/B_{z1} = 3$, $U_{\mathrm{plume}} = 0$ km/s. $t = 0$. (For interpretation of the references to colour in this figure legend, the reader is referred to the Web version of this article.)

and ion density. We also assume here that $n_{\mathrm{e,BG}} = n_{\mathrm{i,BG}}$ and $n_{\mathrm{e,plume}} = n_{\mathrm{i,plume}}$. The same approach for the electron pressure was used successfully in models for the Moon's, Europa's, and Titan's plasma environment (see e.g. Lipatov et al. (2018)) and in the model for transmitted shock propagation in the inner magnetosphere including the ring current and the outer radiation belt presented by Lipatov & Sibeck (Lipatov and Sibeck, 2016). In this case the equations for the time evolution of the temperature for each electron species are reduced to the adiabatic condition.

Modeling presented here employs a simplified configuration for the inner magnetosphere and a step-like fast magnetosonic wave to represent the initial stage of the transmitted impulse front inside the magnetopause. In general, we need to get the information for the initial impulse configuration from multi-point satellite observations or from the global MHD simulations. However, to study the basic physics of the interaction between a transmitted impulse and a plume our simplified approach may be useful. Our modeling may be considered as the basis for subsequent studies of more realistic (observed) impulse dynamics. It is clear that the

validity of our model is limited by the time required for perturbations to propagate backward. However, in the regimes investigated in this paper we did not see any perturbations at the left (input) boundary of the computational domain.

We consider two computational domains with the following dimensions – (a): $DX = 10\ R_E$, $DY = 16\ R_E$, and $DZ = 16\ R_E$; (b): $DX = 10\ R_E$, $DY = 8\ R_E$, and $DZ = 8\ R_E$. Here, we choose $R_E = 6371$ km. Fig. 1 presents an illustration of this computational domain.

In our coordinate system, the X axis is directed away from the Sun, the Y axis points in the direction of Earth's orbital motion and the Z axis completes the right-handed system. Note that the Earth is located outside the computational domain at $x = 0, y = 0, z = 0$.

In our modeling the magnetic field represents the sum of the dipole intrinsic geomagnetic field and other perturbations. We also assume that there is no dipole tilt for the intrinsic magnetic field to keep the simulation results simple. The initial position of the transmitted impulse (step-function magnetic field profile) is shown in Fig. 1 (bottom row).

In our modeling we assumed that the background plasma is homogeneous with a density ≈ 10 cm^{-3} (see e.g. (Moldwin et al., 2002)). We also use a much lower value for background density of 2.0 cm^{-3} which was observed by the Magnetospheric Multiscale mission spacecraft located at the dawn terminator at 20:00:00 UTC on 2016-03-07 (see e.g. (Lipatov et al., 2020)). Our background plasma does not include the outer radiation belt, ring current and plasmasphere. We create a transmitted impulse by imposing a beam entering the left boundary of the computational domain. The initial position of the transmitted impulse (step--function density profile) is shown in Fig. 1 (middle row). We consider a plasmaspheric plume in the form of a cube (rectangular box) with a size $4\ R_E \times 4\ R_E \times 4\ R_E$ and a center located at $y = -2\ R_E$, $x = -10\ R_E$ and $z = 0$.

At the flank boundaries, we apply a damping boundary condition for the electromagnetic field. At the downstream boundary a "Sommerfeld" radiation condition for the magnetic field and a free escape condition for particles has been applied. This boundary condition allows the re-entry of a portion of the particles from the outflow plasma. The upstream values of the magnetic field and electric fields are $\mathbf{B} = \mathbf{B}_0$ and $\mathbf{E} = -\mathbf{U}_0 \times \mathbf{B}_0/c$.

The computational domain contains a grid of $1121 \times 321 \times 321$ points. The initial ion distributions of the background plasma and plasmaspheric plume were approximated by two sets of macro-particles with $\approx 20 - 38$ and $\approx 60 - 250$ macro-particles per cell respectively. A separate set of the macro-particles was continuously generated to simulate the transmitted shock wave with an $\approx 80 - 120$ macro-particles per cell approximation. We guess that the use of $\approx 80 - 120$ macro-particles per cell will be enough to resolve of the general structure of the transmitted shock wave. We have increased this number by a factor of 2 in various modeling runs and results were approximately the same. The hot ions in the transmitted shock wave penetrate into the foot of the shock front and they provide satisfactory particle statistic inside the foot. However, the future modeling needs an adaptive resolution of the shock ramp to take into account the possible ion acceleration by shock surfing and Fermi mechanism. To reduce the numerical "shot" noise we use variable mass macro-particles to generate the initial spatial distribution of the plasmaspheric drainage plume ions (see, e.g. (Lipatov, 2012),). A set of equations (1)–(8) with the boundary and initial conditions described above was used in our modeling. The particle dynamics and electromagnetic field equations were solved with implicit algorithms (Sects. 3.3 and 5.2.4 from Lipatov (2002)).

The numerical time step Δt_p for each particle push is chosen to satisfy the condition $\Delta t_p \leq \min(\Delta x, \Delta y, \Delta z)/(16 * v_{max})$, where v_{max} denotes the maximum value of the macro-particle velocity. The numerical time step Δt_f for the electromagnetic field update is chosen to be $\Delta t_f \approx \Delta t_p/16$. The dimensional time steps are $\Delta t_p \approx 10^{-4}$ s and $\Delta t_f \approx 3 \times 10^{-6}$ s. This particle time step will provide a good numerical approximation of the H^+ ion gyro rotation for a wide range of magnetic field ($\Omega_i \approx 1$ rad/s for $B \approx 10$ nT, $\Omega_i \approx 10^3$ rad/s for $B \approx 10^4$ nT). In the case of heavy ions, for example O^+, a numerical approximation would be better.

The grid spacings are $\Delta_x \approx 60$ km, $\Delta_y \approx 320$ km and $\Delta_z \approx 320$ km. The grid spacing in the x-direction will provide an approximation for spatial scales of several proton inertial lengths $c/\omega_{pi} = 228$ km ($n_{\text{background}} = 1$ cm^{-3}) and $c/\omega_{pi} = 76$ km ($n_{\text{background}} = 10$ cm^{-3}). We use an implicit 3-D hybrid model (see e.g. Lipatov (2002), Lipatov et al. (2002)).

Note that the coupling between the background plasma flow (impulse) and drainage plume ions excites low-frequency resonant and non-resonant waves (Winske et al., 1985) on these scales. The values for the ion gyroradii estimated for speeds corresponding to those at the transmitted shock front ($\approx 900 - 3300$ km/s, see Table 1) are the following: (a) $\rho_{cp} \approx (0.5 - 7) \times 10^3$ km, $\rho_{cO^+} \approx 5.5 \times 10^4$ km for $B = 10$ nT; (b) $\rho_{cp} \approx (1 - 3.6) \times 10^2$ km, $\rho_{cO^+} \approx 5.5 \times 10^3$ km for $B = 100$ nT; (c) $\rho_{cp} \approx (1 - 3.6) \times 10$ km, $\rho_{cO^+} \approx 5.5 \times 10^2$ km. For $B = 1000$ nT. The mesh resolution will underestimate the dimensions of ramp and the foot of the shock wave (impulse) in the proton background plasma at the initial stage for regions with $B = 10$ nT. At later times the impulse becomes more dispersive and the shock front may lose its thin structure. The spatial scale already exceeds the proton gyroradius due to mass loading with the drainage plume ions.

In our simulation of the interaction between the transmitted impulse and the plasmaspheric plume we have adopted the following initial sets of transmitted shock and background parameters in accordance with observations: the values of $U_{\text{downstream}} = U_0$ are in the range from 600 km/s to 2000 km/s; initial thermal velocity $v_{\text{th,downstream}} = 200$ km/s and density in the region downstream from the shock $n_{\text{shock}} = 40$ cm^{-3} or $n_{\text{shock}} = 6$ cm^{-3}; initial background plasma thermal velocity and density $v_{\text{th,BG}} = 20$ km/s and $n_{\text{BG}} = 10$ cm$_{-3}$ or $n_{\text{BG}} = 2$ cm^{-3}; the value of the transmitted magnetic field at the outer boundary ($x = -14\ R_E$) $B_0 = 10.0$ nT. Ion energy measurements in plasmaspheric plumes demonstrate the sporadic appearance of cold ions (10 eV) (Zhang et al., 2012). In our model we use cold ions in the initial plume configuration. Note that we have performed preliminary modeling for a wide range of bulk velocities downstream from the impulse and density jumps.

3. Modeling results

The structure of the collisionless shock wave front is a key factor for understanding particle heating and acceleration inside in the drainage plume, radiation belts and the ring current. We have performed preliminary modeling for a wide range of bulk velocities downstream from the impulse and density jumps and we now discuss how the input parameters affect the results. The main results are summarized in Table 1.

3.1. Interaction between transmitted impulse and the plasmaspheric plume for a fast moving impulse front

In this scenario the initial bulk velocity downstream from the impulse is about 2000 km/s, while the density jump is about 4, so the speed of the impulse front is about $U_{\text{shock}} \approx 3200$ km/s (case 1a, Table 1). Fig. 1 shows the initial distributions for the background plasma, plume density and the perturbation in the magnetic field. Fig. 1 shows the planer impulse entering the simulation domain from the sunward (-X) side.

While the transmitted impulse propagates through the outer dayside magnetosphere, the impulse front interacts with particles in the plume. The portion of the transmitted impulse outside of the plume propagates freely. Fig. 2 present 2-D cuts of the plasma density profile for the background (Fig. 2 (g)) and plume (Fig. 2 (h, j)) plasma, and variations in the electric (Fig. 2 (b, c)) and magnetic (middle column) field ($\mathbf{B}-\mathbf{B}_{\text{dipole}}$) (Fig. 2 (d - f)) produced in the 3-D global hybrid model at time $t \approx 20.02$ sec.

One can see spatially dependent structure of the reverse and forward shock fronts. The forward shock propagates more slowly inside than

Table 1
Parameters of the impulses. $\beta_{plume} = 0$. Spatial numerical resolution is $\Delta_x \approx 60$ km.

Case	U_0(km/s)	β_p	N(cm^{-3})	R_{ci}(10^2 km)	Δ_{sh}(10^2 km)	$\frac{T_{\perp,Shock}}{T_{\parallel,Shock}}$	$\frac{N_2}{N_1}$ and $\frac{B_2}{B_1}$ jumps at forward shock
	U_{sh}(km/s)	β_e	B(nT)	$\frac{c}{\omega_{pi}}$(10 km)	λ_x(10^3 km)	$\frac{T_{\perp,Plume}}{T_{\parallel,Plume}}$	reverse shock
1a	2000	0.1 – 0.2	10 – 100	2 – 20	≈ 3.2	≈ 4 – 9	≈ 5 – 8, ≈ 6 – 13
	3155 – 3300	0.01 – 1	10 – 100	2.5 – 7.6	≈ 2.4 – 3 (H_2^+)	≈ 13 – 18	≈ 2.5, ≈ 8
1b	2000	0.1 – 0.2	2 – 18	1 – 10	≈ 3.2	≈ 5	≈ 5 – 7, ≈ 12 – 13
	3155 – 3300	0.01 – 1	4 – 9	5 – 15	≈ 2.4 – 3 (H_2^+)	≈ 13 – 18	≈ 3, ≈ 2 – 3
2	1000	0.1 – 0.2	10 – 100	1 – 10	≈ 4	≈ 5 – 7	≈ 4, ≈ 6
	1600 – 1300	0.01 – 1	10 – 100	2.5 – 7.6	≈ 3 – 4	≈ 4 – 8	≈ 2.75, ≈ 6
3	600	0.1 – 0.2	10 – 100	0.6 – 6	≈ 12	≈ 7 – 12	≈ 3.2, ≈ 4.5 – 6
	700 – 900	0.01 – 1	10 – 100	2.5 – 7.6	≈ 1.7 – 2.3	≈ 6 – 12	≈ 2.55, ≈ 4

outside of the plume. The front deceleration is caused by mass loading with the plume ions (see Fig. 2, (g)). The reverse front is much stronger inside than outside the plume (see red arrow in Fig. 2 (g)). We suggest that the formation of the reverse shock is due to the increasing geomagnetic field strength encountered as the transmitted impulse propagates deeper inside the inner magnetosphere. At some critical point the transmitted impulse creates a local mini-magnetosphere with a bow-shock like reverse shock and a forward front. The separatrix (the interface between the forward and reverse shock downstream regions) serves as the local magnetopause. As will be shown in Section 3.4, the reverse

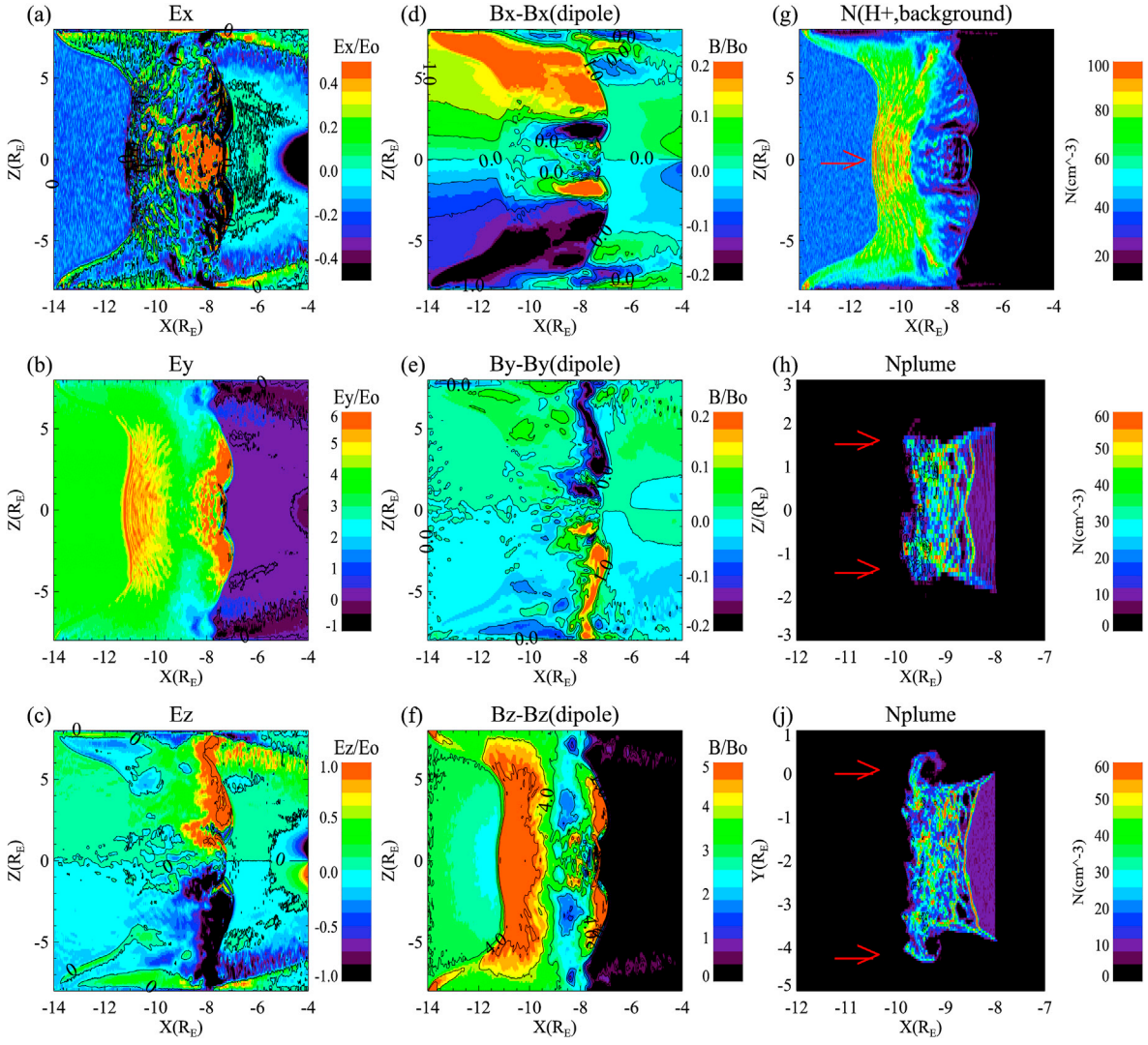

Fig. 2. After the passage of the shock. 2-D cuts of background ion density (g), plume ($M_i = 2M_p, Z = +1$) density (h, j), magnetic field (**B**−**B**$_{\text{dipole}}$) (d, e, f) and electric field (a, b, c) profiles in x-y and x-z planes in case 1a (Table 1). $U_0 = 2000$ km/s. $U_{\text{plume}} = 0$ km/s. $t \approx 20.02$ sec. Red arrow shows the location of the reverse shock in the background density (top, right) and the beams from the plume (middle, right) and (bottom, right). The cuts for the plume density are represented here on a small scale. (For interpretation of the references to colour in this figure legend, the reader is referred to the Web version of this article.)

shock was observed even when the drainage plume was absent, however, the inclusion of the dense and extended plume with a density ($10-200 cm^{-3}$) may change the local structure of the transmitted impulse. Such modeling will be discussed in future publications.

Let us consider the dynamics of the plume while it interacts with the transmitted shock. Fig. 2 (h, j) shows 2-D cuts of the perturbations in the plume density profile. One can see a strong deformation of the plume. The lobe side of the plume moves from an original position at $x = -12\ R_E$ to a position at $x = -10\ R_E$ (see red arrows in Fig. 2 (b, c)). The plume becomes non-symmetric in the $y-z$ plane due to the plume ion dynamics with an anisotropic velocity distribution function. It will also be noted that a portion of the overheated ions from the lobe side creates strong beams which move across the magnetic field (see red arrows in the $x-y$ plane in Fig. 2, (j)).

Next we analyze the wave-particle interactions upstream and downstream from the transmitted impulse (shock). The structure of the collisionless shock wave front may be a key factor for understanding particle heating and acceleration inside magnetospheric plasma structures. Fig. 3 shows the time dependent 1-D impulse and plume structures along the line ($y = -2\ R_E$ at $z = 0$). The modeling demonstrates the formation of a forward-reverse shock structure inside the transmitted impulse with forward and reverse shock fronts which developed from the initial step-like density profile [Fig. 3, row (a)]. One can see the formation of the separatrix ($x \approx -10.3\ R_E$ at time $t = 17.16$ sec) which separates the regions downstream from the forward and reverse shocks. The reverse shock front ("RSH") has a strong density jump ($N_2/N_1 \approx 2.5$) whereas the very dynamic forward shock front has an even greater density jump ($N_1/N_0 \approx 5-8$) and a high speed of $U_{front} \approx 3300$ km/s. The typical thickness of the forward front in this case is about 3×10^2 km. During the deformation of the plume, several peaks occur in the plume density profile [Fig. 3, row (b)]. The typical distance between the peaks is about 3×10^3 km. The plume density inside the peaks reaches values of about 60–100 cm^{-3} in good agreement with observation ((Zhang et al., 2012), Fig. 4 (f)). At this time the THEMIS A spacecraft was at a distance of $\approx 8\ R_E$ from the Earth. At later times ($t \approx 20.02$ sec) the forward shock

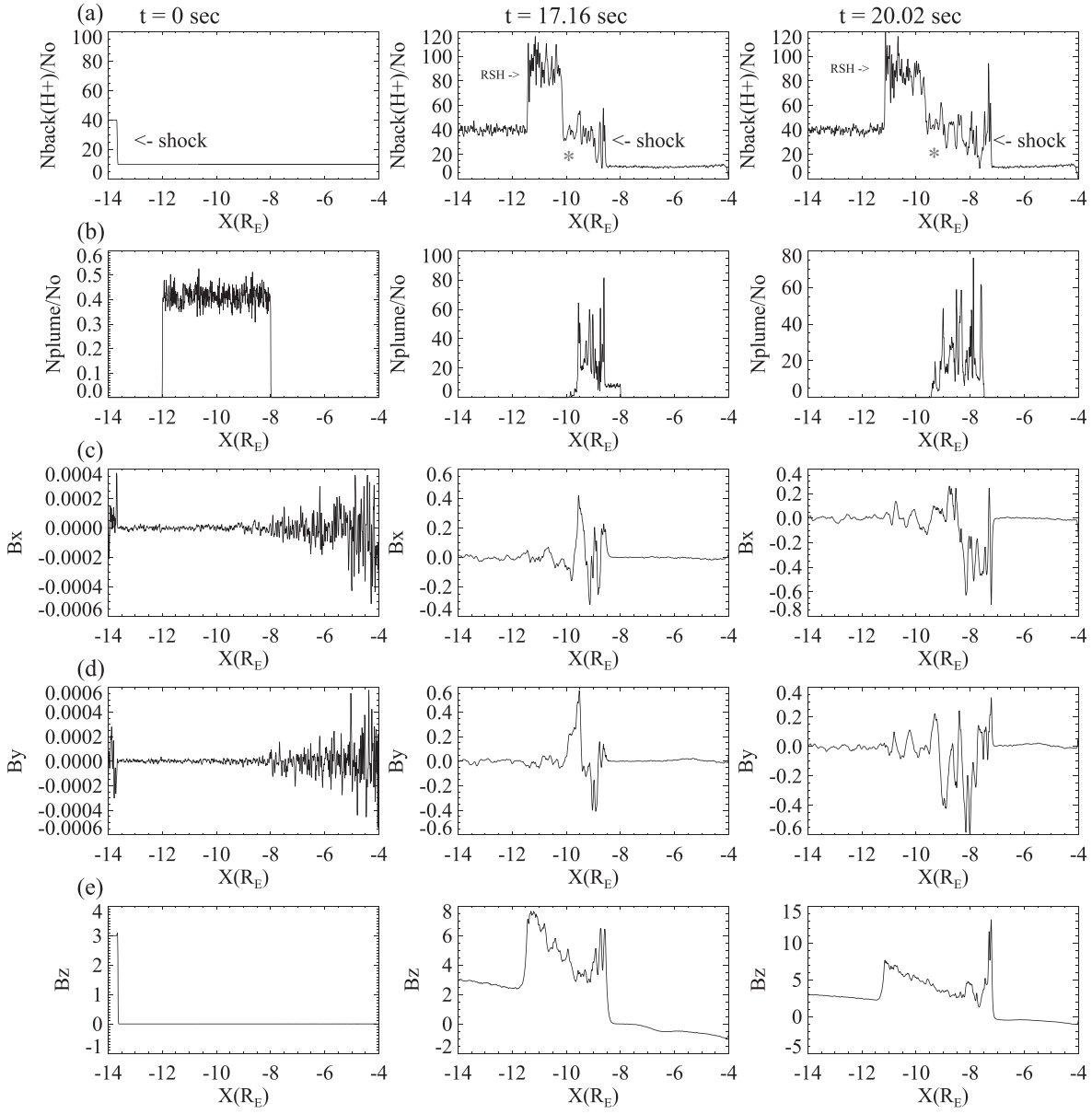

Fig. 3. Shock (a) and plume (b) time dependent structures in case 1a (Table 1). $U_{downstream} = 2000$ km/s, $N_2/N_1 = 4$, $B_{z2}/B_{z1} = 3$, $U_{plume} = 0$ km/s. Profiles in (c, d, e) show perturbations in B_x/Bo, B_y/Bo, and B_z/Bo components. "RSH" and "shock" denote shock front and reverse shock. Red star denotes the position of the separatrix between forward and reverse shocks.

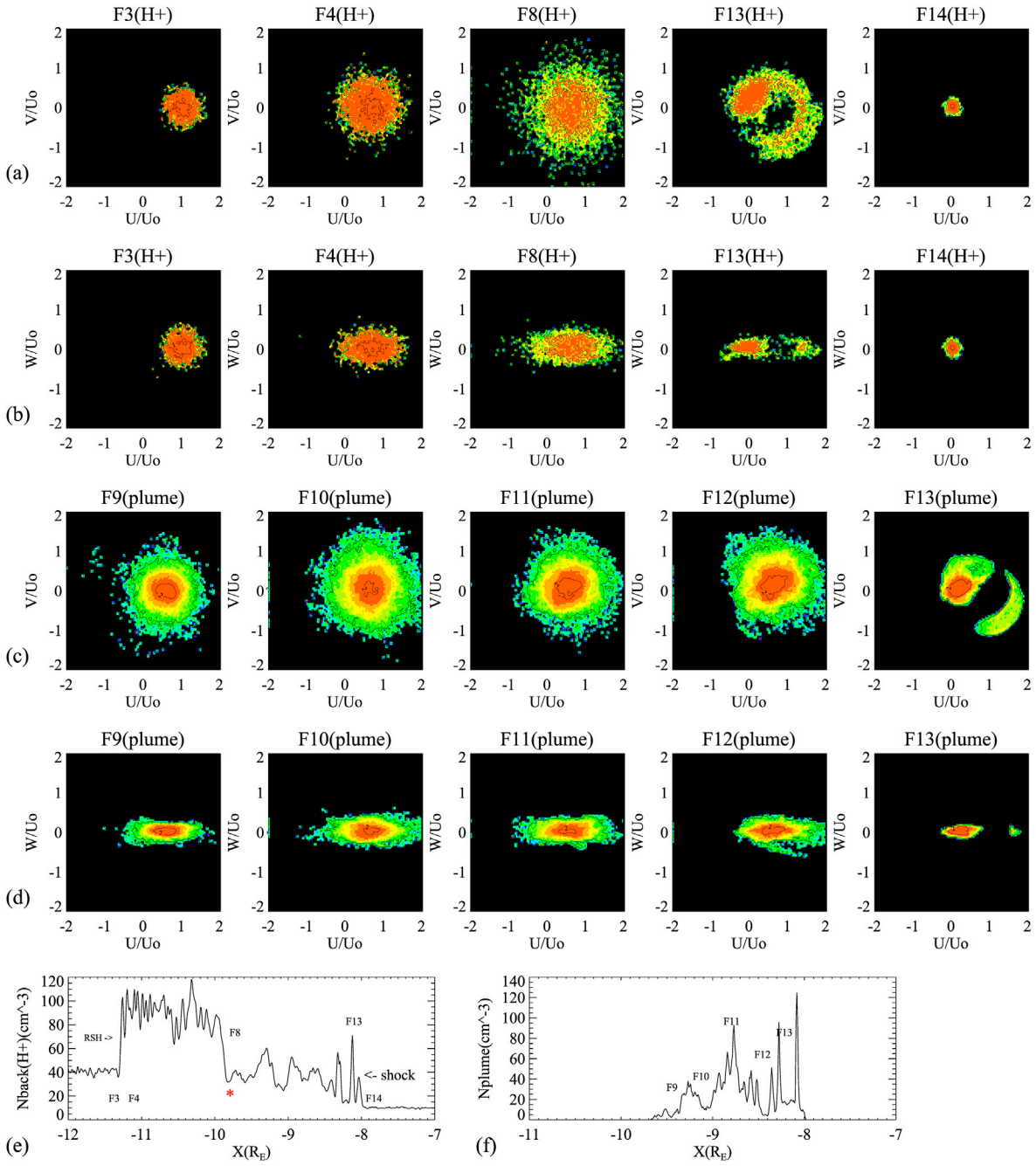

Fig. 4. Non-Maxwellian ion velocity distribution functions (VDFs) for the background (H^+) (rows (a) and (b)) and plume ($M_i = 2M_p, Z = +1$) (rows (c) and (d)) plasma at $t = 18.59$ sec in case 1a (Table 1). The spatial location of the VDFs shown with the numbers in the 1-D cut of the background (Fig. (e)) and plume (Fig. (f)) density profiles. The passage of the shock generates non-Maxwellian velocity distribution functions that can trigger waves and instabilities. This figure shows anisotropic ion velocity distributions downstream from the forward and reverse shock fronts. The velocities V and U are perpendicular to the geomagnetic field whereas the velocity W is parallel to the geomagnetic field. $U_{\text{downstream}} = U_0 = 2000$ km/s. Red star denotes the position of the separatrix between forward and reverse shocks. (For interpretation of the references to colour in this figure legend, the reader is referred to the Web version of this article.)

front is located outside the drainage plume and it becomes stronger with the formation of an overshoot in the density profile of about $N_2/N_1 \approx 8.8$ (Fig. 3, row(a), right column). The speed of the front is about 3155 km/s. The modeling was stopped when the impulse's front passed the right initial boundary of the plume.

The magnetic field perturbation profiles are shown in Fig. 3 (c), (d) and (e). The main component of the magnetic field B_z has two overshoots at the forward and reverse shock fronts (Fig. 3, (e) row, middle and right columns). The forward shock front scale (Δ_{sh}) is about 320 km. The values of the magnetic field (B_z) in the overshoot are 7 B_0 at time $t = 17.6$ sec and 14 B_0 at time $t = 20.02$ sec. Fig. 3 (c) and (d) shows a strong perturbation in the B_x and B_y magnetic field components along the x axis. The values of these perturbation are about $\Delta B \approx 0.4 - 0.6B_0$ and the spatial scales of these perturbations are about $(2-3) \times 1000$ km.

Fig. 4 shows the formation of an anisotropic ion velocity distribution function (VDF) in the transmitted impulse (rows (a) and b) and drainage plume (rows (c) and (d)) at various positions along the x axis. Here $y = -3\ R_E$ and $z = 0$. The spatial locations of these VDF's along the x axis are marked in the density profiles of the ions from the transmitted impulse Fig. 4 (e) and plume 4 (f).

Strong variations in the ion VDF's are observed in the region between

the reverse (point - F4) and forward (point - F14) shock fronts. One can see the anisotropic VDF's of the background and plume ions. Near the forward shock front (point - F13) one can seen the core of the heated background ions and the halo of transmitted or reflected and then transmitted ions at the forward shock front. The heated ion core represents a mixture of the background cold ions from the region upstream of the forward shock and heated ions from the region downstream. The energetic part of the ions circulates near the shock front providing the fluctuations in the density profile (Fig. 4, e). In the middle of the transition between forward and reverse shock fronts (red star near the point F8 - separatrix surface in the bottom panel) one can see quasi-Maxwellian ion VDF's due to phase mixing, see Fig. 4 (rows (a) and (b)). The value of the background ion temperature anisotropy varies from $T_{\perp,Shock}/T_{\parallel,Shock} \approx 4$ to $T_{\perp,Shock}/T_{\parallel,Shock} \approx 9$.

Let us consider the dynamics of the plume ions. Mass loading of the plume ions causes the latter to form anisotropic VDF's (Fig. 4, rows (c) and (d)). The drainage plume ions gain maximum energy between points F10 and F12. Just behind the forward shock front (point F13 in Fig. 4, rows (c) and (d)) one can see an anisotropic quasi-Maxwellian core and halo of the drainage plume ion which form due the interaction with the forward shock front. Note that this ion VDF looks likes the background ion VDF just behind the forward shock front (point F13 in Fig. 4, rows (a) and (b)). At the same time the value of the drainage plume ion temperature anisotropy varies from $T_{\perp,Plume}/T_{\parallel,Plume} \approx 13$ (point F12, Fig. 4, rows (c, d) and (f)) to $T_{\perp,Plume}/T_{\parallel,Plume} \approx 16$ (point F9, Fig. 4, rows (c, d) and (f)) at time $t = 18.59$ sec. Such anisotropic ion velocity distributions can trigger the ballooning-mirror instability (Cheng and Qian, 1994; Cheng et al., 1994; Zhu et al., 2009; Korotova et al., 2013). THEMIS-A observations confirmed the formation of anisotropic energetic ring current ions distribution (see Fig. 4, bottom from Zhang et al. (2012)), with energies of a few tens keV. Such anisotropic ion velocity distributions possibly can excite EMIC waves.

We have also modeled much weaker jumps in the density and magnetic field at the front of the transmitted impulse. The following parameters were used in this modeling: background density, $N_0 = 2$ cm^{-3}; an initial jump in the density at the front of the transmitted impulse, $N_0 = 6$ cm^{-3}; an initial jump in the magnetic field at the front of impulse, $B = 3\,B_0$; and downstream velocity, $W_0 = 2000$ km/s (case 1b, Table 1). The initial thickness of the plume in y and z direction is 1.0 R_E.

Fig. 5 shows the effects of the drainage plume on the shock structure. The modeling demonstrates a formation of small perturbations in the electromagnetic field profiles and in the background density due to the

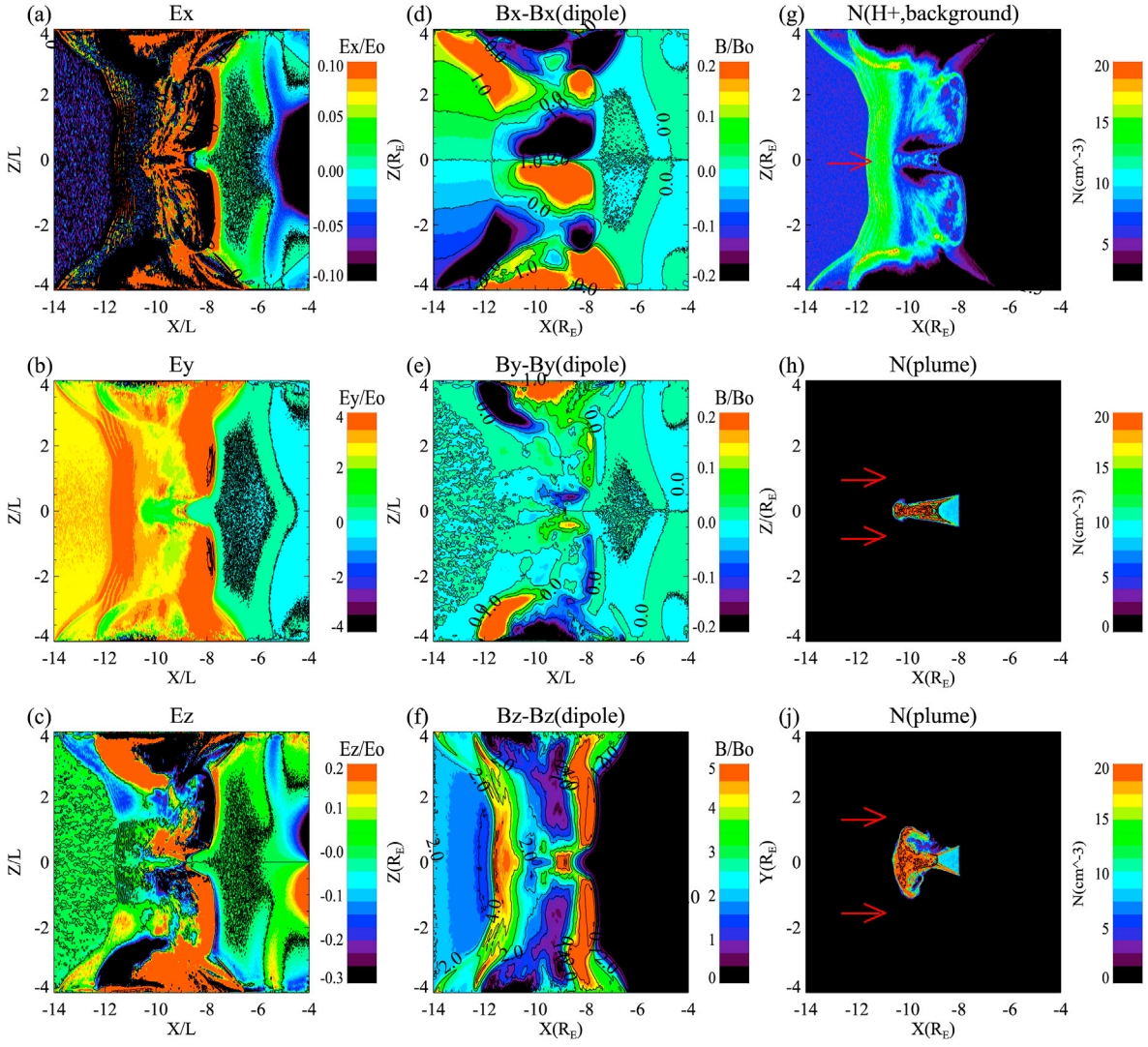

Fig. 5. After the passage of the shock. 2-D cuts of background ion density (a), plume ($M_i = 2M_p, Z = +1$) density (h, j), magnetic field ($\mathbf{B}-\mathbf{B}_{\text{dipole}}$) (d, e, f) and electric field (a, b, c) profiles in x-y and x-z planes in case 1b (Table 1). $U_0 = 2000$ km/s. $U_{\text{plume}} = 0$ km/s. $t \approx 14.01$ sec. Red arrow shows the location of the reverse shock in the background density (g) and the beams from the plume (h) and (j). (For interpretation of the references to colour in this figure legend, the reader is referred to the Web version of this article.)

small dimensions of the plume in the y and z directions. However, the perturbations in the plume configuration in the y direction are more significant than those in Fig. 2. Fig. 6 shows the evolution of the 1-D cuts in the background and plume density profiles, as well as the 1-D cuts in the magnetic field profiles. This figure confirms the formation of the forward and reverse shocks due to shock propagation in the dipole type magnetic field.

3.2. Interaction between transmitted impulse and the plasmaspheric plume for a moderately fast moving impulse front

In this case 2 (Table 1) the initial bulk velocity downstream from the impulse is about 1000 km/s, while the density jump is about 4, so the speed of the impulse front is about $U_{\text{shock}} \approx 1044$ km/s. The time evolution of 1-D cuts for the transmitted impulse and drainage plume structures in this case differs from that for case 1a (Table 1) with $U_0 =$ 2000 km/s. From $t = 0$ to $t = 34.32$ sec the modeling shows the formation of a two-shock structure with a weaker jump in the density at the forward shock front.

By $t = 34.32$ sec the modeling clearly demonstrates the formation of a surface (separatrix) which separates the downstream regions of the forward and reverse shocks at $x \approx -10.\ R_E$. At the $t = 40.04$ sec the separatrix has a more diffusive structure and is located at $x \approx -9.5\ R_E$. At $t = 34.32$ sec the compression downstream from the reverse shock ($N_2/N_1 \approx 1.75$ and $N_{overshoot}/N_1 \approx 2.75$) is lower than in the case for $U_0 = 2000$ km/s ($N_2/N_1 \approx 2.5$). The compression downstream of the forward shock is approximately the same (($N_2/N_1 \approx 4$.) Later at $t =$ 40.04 sec, the reverse shock structure becomes more irregular with strong oscillations near the shock front. The forward shock had a much weaker density jump, an overshoot, and the speed of its front is about 1241 km/s.

The main component of the magnetic field B_z has two overshoots at the forward and reverse shock fronts The forward shock front scale thickness (Δ_{sh}) is about 400 km. The peak values for the perturbations in the magnetic field$t = 17.6$ near the overshoot are 6 B_0 at time sec and 8 B_0 at time $t = 20.02$ sec. The modeling shows a strong perturbation in

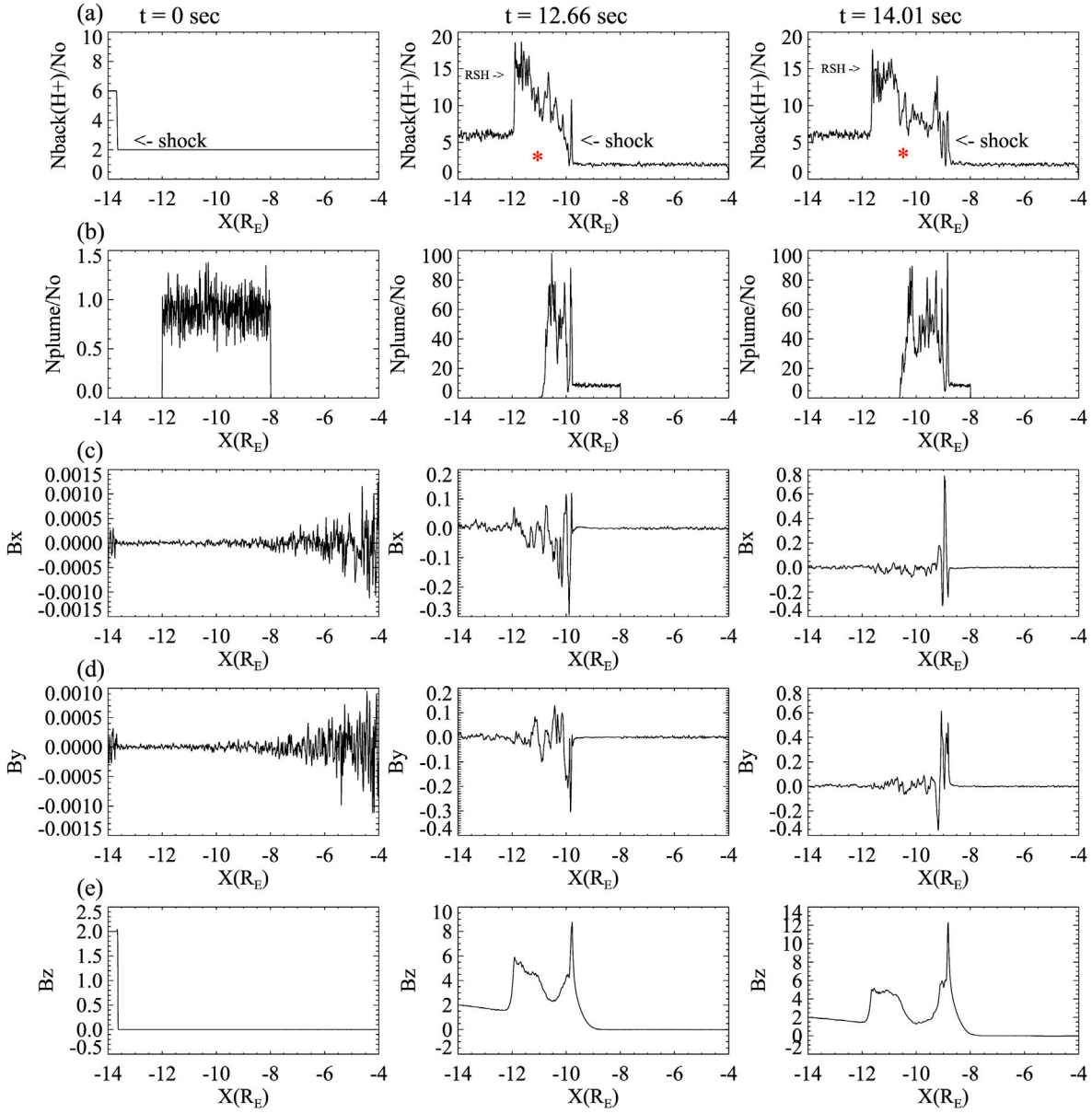

Fig. 6. Shock (a) and plume (b) ($M_i = 2M_p, Z = +1$) time dependent structures in case 1b (Table 1). $U_{\text{downstream}} = 2000$ km/s, $N_2/N_1 = 3$, $B_{z2}/B_{z1} = 2$, $U_{\text{plume}} = 0$ km/s. Profiles in (c, d, e) show perturbations in B_x/Bo, B_y/Bo, and B_z/Bo components. "RSH" and "shock" denote shock front and reverse shock. Red star denotes the position of the separatrix between forward and reverse shocks.

the B_x and B_y magnetic field components along the x axis. The values of these perturbation are about $\Delta B \approx 0.2 - 0.5 B_0$ and the spatial scales of these perturbations are about $(3-4) \times 1000$ km.

Let us consider now VDF's of the background and drainage plume ions in the case with $U_0 = 1000$ km/s. The modeling shows the formation of the anisotropic ion velocity distribution functions (VDF) in the transmitted impulse along the x axis. Here $y = -3\ R_E$ and $z = 0$. The spatial locations of these VDF's along the x axis are marked in the density profiles of the ions from transmitted impulse (e) and plume (f) correspondingly.

Behind the forward shock front we can seen the core of the heated background ions and the halo of transmitted or reflected and then transmitted ions at the forward shock front. In the middle of the transition between forward and reverse shock fronts one can see quasi-Maxwellian ion VDF's due to phase mixing. The value of the background ion temperature anisotropy varies from $T_{\perp,Shock}/T_{\|,Shock} \approx 5.7$ to $T_{\perp,Shock}/T_{\|,Shock} \approx 7.1$. The value of the drainage plume ion temperature anisotropy varies from $T_{\perp,Plume}/T_{\|,Plume} \approx 4.6$ to $T_{\perp,Plume}/T_{\|,Plume} \approx 7.7$. The observed ion VDF temperature anisotropies may excite the ion cyclotron instability.

3.3. Interaction between transmitted impulse and the plasmaspheric plume for a slow moving impulse front

In case (3) (Table 1) the impulse structure and deformation of the drainage plume were studied for an impulse initial velocity $U_0 = 600$ km/s. In this case the profile of the transmitted impulse differs from the cases with $U_0 = 2000$ km/s and $U_0 = 1000$ km/s. The forward-reverse shock structure demonstrates a strong evolution in time. Here, we cannot identify a distinct location for the separatrix which separates the regions downstream of the forward and reverse shocks but we can indicate the approximate location of this surface near $x \approx -10.5\ R_E$ at $t = 52.47$ sec. At later times the separatrix was more diffusive than described in Sects. 3.1 and 3.2 and it is located at $x = -10.3\ R_E$ at $t = 62.01$ sec.

At time $t = 52.47$ sec the compression downstream of the reverse shock ($N_2/N_1 \approx 1.66$ and $N_{overshoot}/N_1 \approx 2.55$) is lower than it was in the case with $U_0 = 2000$ km/s ($N_2/N_1 \approx 2.5$). The compression downstream of the forward shock is also lower ($N_2/N_1 \approx 3.$). The speed of the forward front is about 670 km/s. At the later time $t = 62.01$ sec the reverse shock structure becomes more irregular with strong oscillations near a shock front. At time $t = 52.47$ sec the compression downstream from the reverse shock is $N_2/N_1 \approx 2.1$ and $N_{overshoot}/N_1 \approx 3.2$ which are lower than was observed in the case with $U_0 = 2000$ km/s ($N_2/N_1 \approx 2.1$). The compression downstream from the forward shock is also lower ($N_2/N_1 \approx 3.$). The forward shock has a much weaker density jump and overshoot. The speed of the forward front is about 870 km/s.

The main component of the magnetic field B_z has two overshoots at the forward and reverse shock fronts. The forward shock front scale (Δ_{sh}) is about 1200 km. The perturbations in the magnetic field near the overshoot are 4.5 B_0 at time $t = 52.47$ sec and 6 B_0 at time $t = 62.01$ sec. The values of these perturbation are about $\Delta B \approx 0.2 - 0.3\ B_0$ and the spatial scales of these perturbations are about $(1.7-2.3) \times 1000$ km.

Let us consider now VDF's of the background and drainage plume ions in this case ($U_0 = 600$ km/s). The modeling shows the formation of the anisotropic ion velocity distribution function (VDF) in the transmitted impulse and drainage plume. Although, the general picture of VDF's looks approximately like that of the VDF's in cases with $U_0 = 2000$ km/s and $U_0 = 1000$ km/s, there are important differences in these pictures. The plume ion energy which is determined by the bulk velocity in the region downstream from the transmitted impulse is much smaller in the present case so that pickup ions gain much less energy.

Strong variations in the background ion VDF's are observed in the region between the reverse and forward shock fronts. One can see the anisotropic VDF's of the background ions. Behind the forward shock front one can seen the core of the heated background ions and the halo of transmitted or reflected and then transmitted ions at the forward shock front. In the middle of the transition between forward and reverse shock fronts one can see quasi-Maxwellian ion VDF's due to phase mixing at the location of the separatrix surface. The background ion temperature anisotropy varies from $T_{\perp,Shock}/T_{\|,Shock} \approx 7$ to $T_{\perp,Shock}/T_{\|,Shock} \approx 12$.

Let us consider the plume ion VDF's dynamics. The plume ion temperature anisotropy varies in the range from $T_{\perp,Plume}/T_{\|,Plume} = 6.2$ to $T_{\perp,Plume}/T_{\|,Plume} = 12.7$. Behind the forward shock front, the plume ion VDF represents a combination of an anisotropic quasi-Maxwellian core and a halo of ions accelerated at the forward shock front.

3.4. Effects of the plume and background electron beta on the impulse structure

Global modeling for the interaction of a transmitted impulse and the drainage plume shows that there are large differences between the plasma and magnetic field structures propagating inside and outside plumes (see e.g. Fig. 3). To study the effects of the plume on the impulse structure we have simulated the following 4 cases; (a) ($M_i = 2M_p, Z = +1$) plasmaspheric plume and the background electron is of about β_e is of about 0.1; (b) No plume and the background electron β_e is about 0.1; (c) No plume and the background electron β_e is about 1, and the initial jump in the density is about 4; (d) No plume and the background electron β_e is about 1, and the initial jump in the density is about 3.

Fig. 7 shows the time dependent structures for each case. One can see that in all cases the propagating impulses exhibit the forward and reverse fronts. The modeling also shows a significant difference in the impulse structures in cases (a) and (b). First of all the shock front propagates faster in case (b) ($U_{sh} \approx 2450$ km/s) then in case (a) ($U_{sh} \approx 1640$ km/s) resulting in much stronger widening of the impulse spatial scale in case of impulse propagation without any plume.

The modeling of the impulse propagation in the case of the higher background electron beta ($\beta_e \approx 1$) shows a significant reduction in the impulse density profile due to the differences in the shock front speed (see e.g. Fig. 7 (c) ($U_{sh} \approx 2750$ km/s) and (d) ($U_{sh} \approx 2600$ km/s)). The jumps in the density profiles are ≈ 2 at the reverse shock front and $\approx 5-6$ at the forward shock front. The forward shock front propagates faster in these (c) and (d) cases with $\beta_e = 1$.

4. Conclusions

Initial results from a hybrid kinetic model for the interaction of transmitted impulses with a simplified configuration for plasmaspheric plumes demonstrates several features:

- 1. A forward-reverse shock structure with forward and reverse shock fronts develops from the transmitted impulse's initial step-like density profile. The formation of a reverse shock was also observed early in the simulation of Lipatov & Sibeck (Lipatov and Sibeck, 2016) but they concluded that this reverse shock was probably associated with the ring current. Our current investigation with or without a plasmaspheric plume found the formation of a forward-reverse shock structure during the propagation of an impulse through the dipole magnetic field. Confirmation of the formation of such structures in the inner magnetosphere requires multi-point observations. The formation of forward-reverse shock pairs has also been observed in the solar wind, for example by the MMS (Cohen et al., 2019) and Ulysses spacecrafts (Ho et al., 1998).
- 2. The passage of the impulse generates anisotropic non-Maxwellian velocity distribution functions (VDF's) in the transmitted plasma and plume ions. Those anisotropic ion VDF's are associated with a strong compression across the magnetic field at the front of the transmitted impulse. They were observed by THEMIS A during a passage of the interplanetary shock wave (Zhang et al. (2012)).

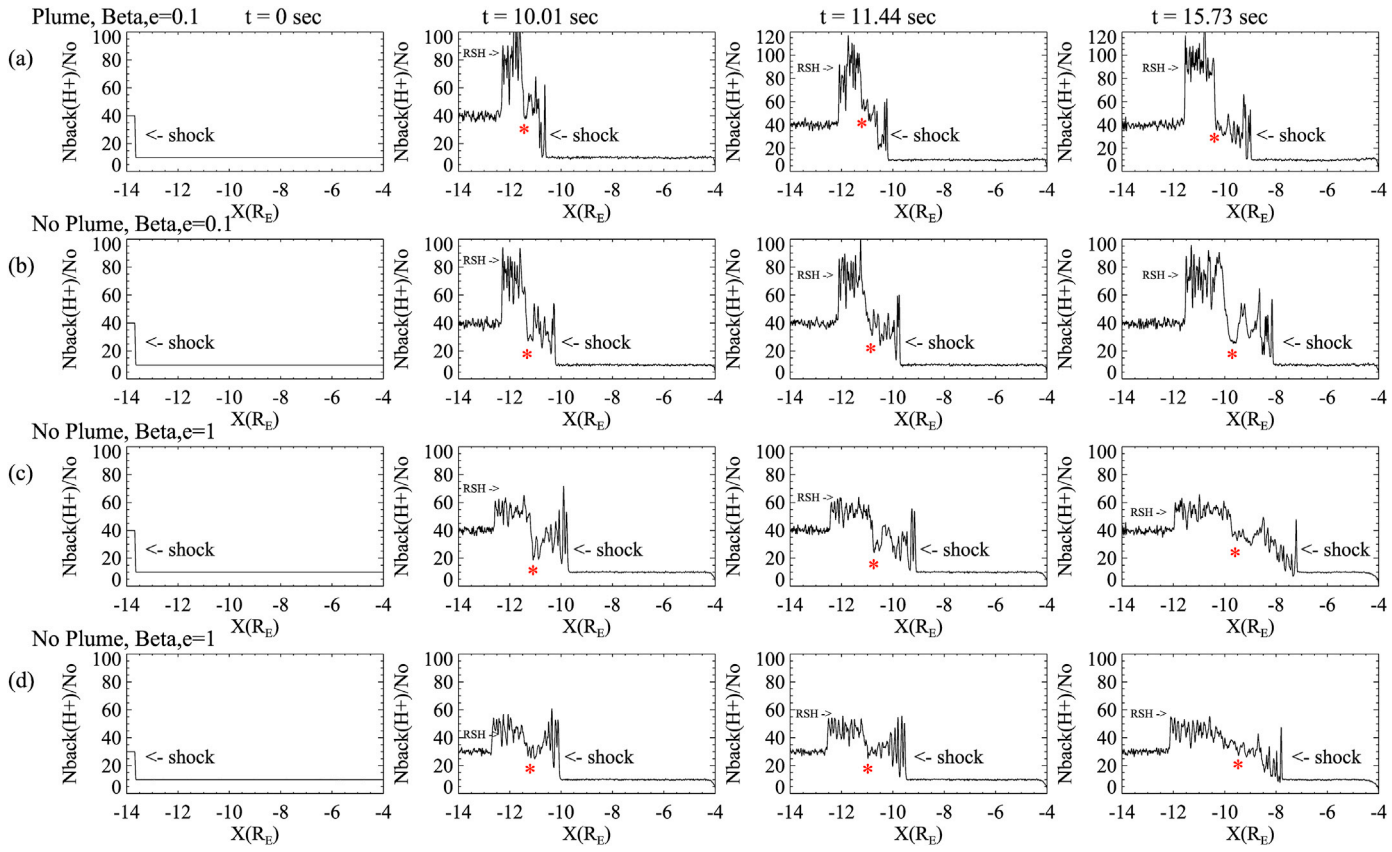

Fig. 7. Effect of plume on shock structures. $U_0 = 2000$ km/s. Plume - ($M_i = 2M_p, Z = +1$). Time dependent background density profiles: (a) With plume, case 1a (Table 1): (b) No Plume. $\beta_e = 0.1$, $n_2/n_1 = 4$; (c) No Plume. $\beta_e = 1$, $n_2/n_1 = 4$; (d) No Plume. $\beta_e = 1$, $n_2/n_1 = 3$. $U_{\text{downstream}} = 1000$ km/s. "RSH" and "shock" denote reverse shock and forward shock front. Red star denotes the position of the separatrix between forward and reverse shocks. (For interpretation of the references to colour in this figure legend, the reader is referred to the Web version of this article.)

- 3. The observed anisotropy of the ion pressure across and along the magnetic field (from 5 to 10) may be further investigated for possible EMIC wave and other instabilities (e.g. mirror-ballooning instability).
- 4. The transmitted shock produces 3-D strong perturbations in the plume density profile with wavelengths about $\lambda_x \approx 1\ R_E$.
- 5. Following the passage of the shock the plume density increases from an initial value of $n_{plume} \approx 8\ \text{cm}^{-3}$ to values $n_{plume} \approx (60-100)\ \text{cm}^{-3}$. These values are in good agreement with observation by THEMIS A (May 28, 2008, Zhang et al. (2012)).
- 6. The plume reduces the Alfvén speed and effectively increases the Mach number in the transmitted shock (impulse). Further modeling will be performed with realistic topology of the plume including a denser portion of the plume near the plasmapause.
- 7. The high value of the background electron beta may reduce the overshoot jumps in plasma density and magnetic field at the forward and reverse shock fronts.

Points 2–5 of the above conclusion are in satisfactory quantitative agreement with the THEMIS observations, so our model is successful.

In future work we expect to model multi-composition drainage plume dynamics during interactions with transmitted impulses and radiation belt electron acceleration during the passage of the transmitted impulses through the inner magnetosphere. We also plan to compare our predictions with observations from the THEMIS and Van Allen Probes spacecraft e.g. the event on October 8, 2013 from Foster et al. (2015). Current spacecraft configurations offer unique opportunities to study the magnetospheric response to interplanetary shocks. These data will provide information about the wave-particle interactions, in particular the heating and acceleration of the particles in the ring current and radiation belts.

Declaration of competing interest

The authors declare that they have no known competing financial interests or personal relationships that could have appeared to influence the work reported in this paper.

Acknowledgments

This work was supported in part by the "Van Allen Storm Probes" and "Magnetospheric Multiscale" NASA missions. Computational resources were provided for the High-End Computational Projects SMD-18-1963 "Shock waves interaction with plasmasphere and radiation belts. Hybrid fluid-kinetic modeling" and SMD-20-87113888 "Plasma physics of multiscale impulsive structures in the magnetosphere. Hybrid fluid-kinetic modeling" by the NCCS (Discover, Goddard) and the NAS (Electra, Ames). A.S.L was also supported in part by NASA Grant 80NSSC20K0146 from SSW-2018 Program (NNH18ZDA001N–C.3) via UMBC. The authors thank the referees for fruitful comments.

Appendix A. Supplementary data

Supplementary data to this article can be found online at https://doi.org/10.1016/j.pss.2020.105104.

References

Anderson, B.J., et al., 1992. A statistical study of Pc 1-2 magnetic pulsations in the equatorial magnetosphere: 2. Wave properties. J. Geophys. Res. 97 (A3), 3089–3101. https://doi.org/10.1029/91JA02697.

Anderson, B.J., Hamilton, D.C., 1993. Electromagnetic ion cyclotron waves stimulated by modest magnetospheric compressions. J. Geophys. Res. 98 (A7) https://doi.org/10.1029/93JA00605, 11,369-11,382.

Angelopoulos, V., 2008. The THEMIS mission. Space Sci. Rev. 141, 5–34. https://doi.org/10.1007/s11214-008-9336-1.

Auster, H.U., Glassmeier, K.H., Magnes, W., Aydogar, O., Baumjohann, W., Constantinescu, D., Fischer, D., Fornacon, K.H., Georgescu, E., Harvey, P., Hillenmaier, O., Kroth, R., Ludlam, M., Narita, Y., Nakamura, R., Okrafka, K., Plaschke, F., Richter, I., Schwarzl, H., Stoll, B., Valavanoglou, A., Wiedemann, M., 2008. The THEMIS fluxgate magnetometer. Space Sci. Rev. 141, 235–264. https://doi.org/10.1007/s11214-008-9365-9.

Borovsky, J.E., Denton, M.H., 2006. Effect of plasmaspheric drainage plumes on solar-wind/magnetosphere coupling. Geophys. Res. Lett. 33, L20101. https://doi.org/10.1029/2006GL026519.

Borovsky, J.E., Welling, D.T., Thomsen, M.F., Denton, M.H., 2014. Long-lived plasmaspheric drainage plumes: where does the plasma come from? J. Geophys. Res. 119, 6496–6520. https://doi.org/10.1002/2014JA020228.

Braginskii, S.L., 1965. Transport processes in a plasma. In: Leontovich, M.A. (Ed.), Reviews of Plasma Physics. Consultants Bureau, New York, pp. 205–240.

Cattell, C., Breneman, A., Colpitts, C., Dombeck, J., Thaller, S., Tian, S., Wygant, J., Fennell, J., Hudson, M.K., Erfun, R., Russell, C.T., Torbert, R., Lindqvist, P.A., Burch, J., 2017. Dayside response of the magnetosphere to a small shock compression: van allen Probes, magnetospheric multiscale, and GOES-13. Geophys. Res. Lett. 44, 8712–8720.

Chappell, C.R., Harris, K.K., Sharp, G.W., 1970. The morphology of the bulge region of the plasmasphere. J. Geophys. Res. 75, 3848.

Chappell, C.R., 1974. Detached plasma regions in the magnetosphere. J. Geophys. Res. 79, 1861.

Cheng, C.Z., Qian, Q., 1994. Theory of ballooning-mirror instabilities for anisotropic pressure plasmas in the magnetosphere. J. Geophys. Res. 99 (A6), 11193–11209.

Cheng, C.Z., Qian, Q., Takahashi, K., Lui, A.T.Y., 1994. Ballooning-mirror instability and internally driven pc 4-5 wave events. J. Geomagn. Geoelectr. 46, 997–1009.

Claudepierre, S.G., Mann, I.R., Takahashi, K., Fennell, J.F., Hudson, M.K., Blake, J.B., Roeder, J.L., Clemmons, J.H., Spence, H.E., Reeves, G.D., 2013. Van Allen Probes observation of localized drift resonance between poloidal mode ultra-low frequency waves and 60 keV electrons. Geophys. Res. Lett. 40, 4491–4497. https://doi.org/10.1002/grl.50901.

Cohen, I.J., Schwartz, S.J., Goodrich, K.A., Ahmadi, N., Ergun, R.E., Fuselier, S.A., Desai, M.I., Christian, E.R., McComas, D.J., Zank, G.P., Shuster, J., Vines, S.K., Mauk, B.H., Decker, R.B., Anderson, B.J., Westlake, J.H., Contel, O.L., Breuillard, H., Giles, B.L., Torbert, R.B., Burch, J.L., 2019. High-resolution measurements of the cross-shock potential, ion reflection, and electron heating at an interplanetary shock by MMS. J. Geophys. Res.: Space Physics. 124, 3961–3978. https://doi.org/10.1029/2018JA026197.

Cornwall, J.M., 1965. Cyclotron instabilities and electromagnetic emission in the ultra low frequency and very low frequency ranges. J. Geophys. Res. 70 (1), 61–69. https://doi.org/10.1029/JZ070i001p0006.

Darrouzet, F., De Keyser, J., Décréau, P.M.E., Lemaire, J.F., Dunlop, M.W., 2006. Spatial gradients in the plasmasphere from Cluster. Geophys. Res. Lett. 33 (8), L08105. https://doi.org/10.1029/2006GL025727.

Darrouzet, F., De Keyser, J., Décréau, P.M.E., Lemdani-Mazouz, F. El, Valliéres, X., 2008. Statistical analysis of plasmaspheric plumes with Cluster/WHISPER observations. Ann. Geophys. 26, 2403–2417.

Darrouzet, F., et al., 2009. Plasmaspheric density structure and dynamics: properties observed by the CLUSTER and IMAGE missions. In: Darrouzet, F., De Keyser, J., Pierrard, V. (Eds.), The Earth's Plasmasphere. A Cluster and Image Perspective. Springer, p. 2009.

Elphic, R.C., Weiss, L.A., Thomsen, M.F., McComas, D.J., Moldwin, M.B., 1996. Evolution of plasmaspheric ions at geosynchronous orbit during times of high geomagnetic activity. Geophys. Res. Lett. 23, 2189.

Engebretson, M.J., Peterson, W.K., Posch, J.L., Klatt, M.R., Anderson, B.J., Russell, C.T., Singer, H.J., Arnoldy, R.L., Fukunishi, H., 2002. Observations of two types of Pc 1-2 pulsations in the outer dayside magnetosphere. J. Geophys. Res. 107 (A12), 1451. https://doi.org/10.1029/2001JA00019.

Foster, J.C., Erickson, P.J., Coster, A.J., Goldstein, J., 2002. Ionospheric signatures of plasmaspheric tails. Geophys. Res. Lett. 29 (13), 1623. https://doi.org/10.1029/2002GL015067.

Foster, J.C., Wygant, J.R., Hudson, M.K., Boyd, A.J., Baker, D.N., Erickson, P.J., Spence, H.E., 2015. Shock-induced prompt relativistic electron acceleration in the inner magnetosphere. J. Geophys. Res. 120 (3), 1661–1674.

Goldstein, J., Sandel, B.R., Thomsen, M.F., Spasojević, M., Reiff, P.H., 2004. Simultaneous remote-sensing and in situ observations of plasmaspheric drainage plumes. J. Geophys. Res. 109, A03202. https://doi.org/10.1029/2003JA010281.

Gosling, J.T., McComas, D.J., Phillips, J.L., Bame, S.J., 1991. Geomagnetic activity associated with earth passage of interplanetary shock disturbances and coronal mass ejections. J. Geophys. Res. 96 (A5), 7831–7839.

Halford, A.J., McGregor, S.L., Murphy, K.R., Millan, R.M., Hudson, M.K., Woodger, L.A., Cattel, C.A., Breneman, A.W., Mann, I.R., Kurth, W.S., Hospodarsky, G.B., Gkioulidou, M., Fennel, J.F., 2015. BARREL observations of an ICME-shock impact with the magnetosphere and the resultant radiation belt electron loss. J. Geophys. Res. Space Physics 120, 2557–2570. https://doi.org/10.1002/2014JA020873.

Ho, C.M., Tsurutani, B.T., Lin, N., Lanzerotti, L.J., Smith, E.J., Goldstein, B.E., Buti, B., Lakhina, G.S., Zhou, X.Y., 1998. A pair of forward and reverse slow-mode shocks detected by Ulysses at 5 AU. Geophys. Res. Lett. 25 (14), 2613–2616.

Korotova, G.I., Sibeck, D.G., Angelopoulos, V., Walsh, B.M., 2013. THEMIS observations of compressional poloidal pulsations in the dawnside magnetosphere: a case study. J. Geophys. Res. 118, 7665–7673. https://doi.org/10.1002/2013JA019360, 2013.

Kress, B.T., Hudson, M.K., Looper, M.D., Lyon, J.G., Goodrich, C.C., 2008. Global MHD test particle simulations of solar energetic electron trapping in the Earth's radiation belts. J. Atmospheric Solar-Terr. Phys. 70, 1727–1737.

Lipatov, A.S., 2002. The Hybrid Multiscale Simulation Technology: an Introduction with Application to Astrophysical and Laboratory Plasmas, Monograph. Springer-Verlag, Berlin, Heidelberg, New York, p. 403.

Lipatov, A.S., 2012. Merging for particle-mesh complex particle kinetic modeling of the multiple plasma beams. J. Comput. Phys. 231, 3101–3118.

Lipatov, A.S., Avanov, L.A., Giles, B.L., 2020. Sub-alfvenic/super-sonic impulsive structures in the magnetosphere. First results from hybrid fluid-kinetic modeling and comparison with MMS observations. Earth and Space Science Open Archive (ESSOAr). https://doi.org/10.1002/essoar.10501844.1 (24 Jan. 2020).

Lipatov, A.S., Motschmann, U., Bagdonat, T., 2002. 3D hybrid simulations of the interaction of the solar wind with a weak comet. Planet. Space Sci. 50, 403–411.

Lipatov, A.S., Sarantos, M., Farrell, W.M., Cooper, J.F., 2018. Effects of multiscale phase-mixing and interior conductance in the lunar-like pickup ion plasma wake. First results from 3-D hybrid kinetic modeling. Planet. Space Sci. 156, 117–129. https://doi.org/10.1016/j.pss.2018.02.017. In: Dust, Atmosphere, and Plasma Environment of the Moon and Small Bodies. Eds. Michal Horany, Allan Stern.

Lipatov, A.S., Sibeck, D.G., 2016. Global effects of the transmitted interplanetary shock wave propagation through the Earth's inner magnetosphere. First results from 3-D hybrid kinetic modeling, Planet. Space Sci 129, 13–23. https://doi.org/10.1016/j.pss.2016.05.010.

Mauk, B.H., Fox, N.J., Kanekal, S.G., Kessel, R.L., Sibeck, D.G., Uhorskiy, A., 2013. Science objectives and rationale for the radiation belt storm Probes mission. Space Sci. Rev. 179, 3–27.

McFadden, J.P., Carlson, C.W., Larson, D., Bonnell, J., Mozer, F.S., Angelopoulos, V., Glassmeier, K.-H., Auster, U., 2008. Structure of plasmaspheric plumes and their participation in magnetopause reconnection: first results from THEMIS. Geophys. Res. Lett. 35 (17), L17S10. https://doi.org/10.1029/2008GL033677.

Moldwin, M.B., Downward, L., Rassoul, H.K., Amin, R., Anderson, R.R., 2002. A new model of the location of the plasmapause: CRRES results. J. Geophys. Res. 107 (A11), 1339. https://doi.org/10.1029/2001JA009211.

Moldwin, M.B., Howard, J., Sanny, J., Bocchicchio, J.D., Rassoul, H.K., Anderson, R.R., 2004. Plasmaspheric plumes: CRRES observations of enhanced density beyond the plasmapause. J. Geophys. Res. Space Physics 109 (A5).

Ober, D.M., Horwitz, J.L., Gallagher, D.L., 1997. Formation of density troughs embedded in the outer plasmasphere by subauroral ion drift events. J. Geophys. Res. 102, 14595–14602.

Roux, C., et al., 1982. Wave-particle interaction near He+ observed on board GEOS 1 and 2: 2. Generation of ion cyclotron waves and heating of He+ ions. J. Geophys. Res. Space Phys. 87, 8174–8190. https://doi.org/10.1029/JA087iA10p08174.

Samsonov, A.A., Sibeck, D.G., Imber, J., 2007. MHD simulation for the interaction of an interplanetary shock with the Earth's magnetosphere. J. Geophys. Res. 112, A12220. https://doi.org/10.1029/2007JA012627.

Samsonov, A.A., Sibeck, D.G., Walsh, B.M., Zolotova, N.V., 2014. Sudden impulse observations in the dayside magnetosphere by THEMIS. J. Geophys. Res. 119, 9476–9496. https://doi.org/10.1002/2014JA020012.

Samsonov, A.A., Sibeck, D.G., Zolotova, N.V., Biernat, H.K., Chen, S.-H., Rastaetter, L., Singer, H.J., Baumjohann, W., 2011. Propagation of a sudden impulse through the magnetosphere initiating magnetospheric Pc5 pulsations. J. Geophys. Res. 116, A10216. https://doi.org/10.1029/2011JA016706.

Sandel, B.R., King, R.A., Forrester, W.T., Gallagher, D.L., Broadfoot, A.L., Curtis, C.C., 2001. Initial results from the IMAGE extreme ultraviolet imager. Geophys. Res. Lett. 28, 1439.

Tsuji, H., Ebihara, Y., Tanaka, T., 2017. Impact of interplanetary shock on ring current ions. In: Proceeding of the JpGU-AGU Joint Meeting 2017, ID: PEM16-P12.

Usanova, M.E., Mann, I.R., Rae, I.J., Kale, Z.C., Angelopoulos, V., Bonnell, J.W., Glassmeier, K.-H., Auster, H.U., Singer, H.J., 2008. Multipoint observations of magnetospheric compression-related EMIC Pc1 waves by THEMIS and CARISMA. Geophys. Res. Lett. 35, L17S25. https://doi.org/10.1029/2008GL034458.

Winske, D., Wu, C.S., Li, Y.Y., Mou, Z.Z., Guo, S.Y., 1985. Coupling of newborn ions to the solar wind by electromagnetic instabilities and their interaction with the bow shock. J. Geophys. Res. 90, 2713–2726.

Young, D.T., Perraut, S., Roux, A., de Villedary, C., Gendrin, R., Korth, A., Kremser, G., Jones, D., 1981. Wave-particle interactions near Ω_{He+} observed on GEOS 1 and 2: 1. Propagation of ion cyclotron waves in -Ω_{He+} rich plasma. J. Geophys. Res. 86 (A8), 6755–6772. https://doi.org/10.1029/JA086iA08p06755.

Zhang, H., Sibeck, D.G., Zong, Q.-G., McFadden, J.P., Larson, D., Glassmeier, K.-H., Angelopoulos, V., 2012. Global magnetospheric response to an interplanetary shock: THEMIS observations. Ann. Geophys. 30, 379–387. https://doi.org/10.5194/angeo-30-379-2012. www.ann-geophys.net/30/379/2012/.

Zhu, P., Raeder, J., Germaschewski, K., Hegna, C.C., 2009. Initiation of ballooning instability in the near-Earth plasma sheet prior to the 23 March 2007 THEMIS substorm expansion onset. Ann. Geophys. 27, 1129–1138, 2009.